Science Bulletin 71 (2026) 2044–2054

Contents lists available at ScienceDirect

Science Bulletin

journal homepage: www.elsevier.com/locate/scib

Article

Large-scale parallel characterization of RNA-guided nuclease activity and specificity

Jitan Zheng [a,b,c,1], Xueyan Wang [a,b,d,1], Mingdi Wu [a,b,c,1], Jing Liu [a,b,1], Hu Feng [a,b,1], Hui Yang [e], Dali Li [f,g], Haoyi Wang [h], Jiazhi Hu [i], Erwei Zuo [a,b,*]

[a] Key Laboratory of Veterinary Pharmaceutical Development, Ministry of Agriculture and Rural Affairs, Lanzhou Institute of Husbandry and Pharmaceutical Sciences, Chinese Academy of Agricultural Sciences, Lanzhou 730050, China
[b] Shenzhen Branch, Guangdong Laboratory for Lingnan Modern Agriculture, State Key Laboratory of Genome and Multi-omics Technologies, Agricultural Genomics Institute at Shenzhen, Chinese Academy of Agricultural Sciences, Shenzhen 518000, China
[c] State Key Laboratory for Conservation and Utilization of Subtropical Agro-Bioresources, College of Animal Science and Technology, Guangxi University, Nanning 530004, China
[d] College of Life Science and Technology, Huazhong Agricultural University, Wuhan 430070, China
[e] Shanghai Institute of Materia Medica, Chinese Academy of Sciences, Shanghai 201203, China
[f] Shanghai Frontiers Science Center of Genome Editing and Cell Therapy, Shanghai Key Laboratory of Regulatory Biology and School of Life Sciences, East China Normal University, Shanghai 200241, China
[g] Shanghai Academy of Natural Sciences (SANS), Shanghai 200031, China
[h] State Key Laboratory of Organ Regeneration and Reconstruction, Institute of Zoology, Chinese Academy of Sciences, Beijing 100101, China
[i] State Key Laboratory of Protein and Plant Gene Research, Genome Editing Research Center, School of Life Sciences, PKU-THU Center for Life Sciences, Peking University, Beijing 100871, China

ARTICLE INFO

Article history:
Received 27 September 2025
Received in revised form 29 January 2026
Accepted 10 March 2026
Available online 23 March 2026

Keywords:
RNA-guided nuclease
Editing efficiency
Off-target effects
Cytotoxicity

ABSTRACT

As systematic comparisons of editing efficiency and specificity seldom keep pace with rapid developments in RNA-guided nucleases (RGNs), the current study examined 50 such editing systems and characterized the off-target effects and genomic structural impacts of a subset of high-efficiency RGNs. Among them, AsCas12a-Ultra, LbCpf1, and AsCas12a-Plus demonstrated similar or higher efficiency compared to SpCas9, while the relatively high efficiency and small size of enOsCas12f1 together support its suitability for *in vivo* delivery. AsCpf1-YH and FnCpf1 exhibited the lowest single-guide RNA-dependent (sgRNA-dependent) off-target risks, whereas DpFNuc showed the highest. Genomic structural analysis revealed that enCas12f-HKRA frequently introduces chromosomal translocations, while Cas12j-SF05 poses a lower risk of such mutations. Notably, the high-efficiency RGNs were associated with translocation hotspots. Additionally, enRhCas12f1 and SpaCas12f1 had the lowest cytotoxicity, while enAsCpf1-HF strongly inhibited cell proliferation. This study establishes the first multidimensional performance evaluation framework for RGNs, providing a data-driven tool to support precise genome editing.
© 2026 The Authors. Published by Elsevier B.V. and Science China Press. This is an open access article under the CC BY license (http://creativecommons.org/licenses/by/4.0/).

1. Introduction

The CRISPR/Cas system, an RNA-guided mechanism for nucleic acid targeting, underpins adaptive immunity in prokaryotes [1]. Since the groundbreaking development of CRISPR/Cas9 for application in gene editing, the field of RNA-guided nucleases (RGNs) has rapidly advanced [2]. The representative type II system, SpCas9, was the first RGN introduced for editing in mammalian cells and has since been extensively applied across various fields [3]. Despite its transformative impacts, from correcting mutations in hemoglobin subunit beta (*HBB*) [4] to engineering agronomic traits, SpCas9 faces several limitations [5], including specific protospacer adjacent motif (PAM) requirements and constraints on its delivery [6]. These challenges have spurred the development of alternative RGNs, such as Cas12a [7] and TnpB systems [8], which offer distinct advantages, although their performance relative to the Cas9 system remains poorly characterized.

The distinct strengths and limitations among these systems highlight their diversity. For example, the Cas12a system employs a simplified RNA guide structure that allows efficient guide RNA synthesis [7]. Additionally, this system can simultaneously target multiple sites by concatenating several protospacers [9]. From a delivery perspective, the compact size of the Cas12f [10] and TnpB nucleases (300–500 amino acids, AA) makes them highly suitable for packaging into delivery vehicles such as adeno-associated

* Corresponding author.
E-mail address: zuoerwei@caas.cn (E. Zuo).
[1] These authors contributed equally to this work.

https://doi.org/10.1016/j.scib.2026.03.047
2095-9273/© 2026 The Authors. Published by Elsevier B.V. and Science China Press.
This is an open access article under the CC BY license (http://creativecommons.org/licenses/by/4.0/).

viruses (AAVs), which are particularly relevant for *in vivo* applications [11]. In contrast, the Fanzor system [12,13], derived from eukaryotic species, displays enhanced capability for nuclear entry, providing a distinct advantage in specific experimental contexts.

Despite the wide array of currently available RGNs, systematic comparisons of their cleavage activity, fidelity, and associated risks remain insufficiently addressed. Moreover, although Cas9 and derivative systems have been thoroughly characterized, the cleavage specificity, insertion/deletion (indel) profiles, and experimental adaptability of many Cas12 and TnpB systems remain inadequately explored [14–17]. This paucity of comprehensive benchmarking has hindered the tailored application and further optimization of these emerging tools across diverse experimental and therapeutic contexts.

To bridge these gaps, in the current study, we conducted a large-scale analysis of 50 RGNs spanning 10 subtypes (including Cas12a [7,18–24], Cas12b [25,26], Cas12e [27], Cas12f [10,28–35], Cas12i [36,37], Cas12j [38–40], Cas12l [41], Cas12n [42], TnpB [8,43] and Fanzor [13,44]) to systematically evaluate their activity, genotoxicity, and cellular impacts. Our findings revealed substantial differences among these RGNs. For instance, AsCas12a-Ultra, LbCpf1, AsCas12a-Plus, and LbCpf1-RVRR exhibited comparable or even higher editing efficiency to that of SpCas9. In particular, we found that, despite its compact structure, enOsCas12f1 showed high efficiency, supporting its suitability for delivery in therapeutic applications. Furthermore, RGNs such as Cas12j-SF05 introduced relatively few sgRNA-dependent off-target effects and chromosomal translocations, underscoring their specificity for precision applications. Conversely, enRhCas12f1 and SpaCas12f1 had the least impact on cell viability. These findings establish a robust framework for strategic selection of gene-editing tools that are tailored to specific research or application requirements, ensuring an optimal balance between efficiency and specificity. This large-scale, parallel evaluation of 50 RGNs, focusing on their editing efficiency, off-target activity, structural genomic impact, and cytotoxicity, can thus guide editing system selection for specialized research or biomedical applications.

2. Materials and methods

2.1. Plasmid construction

To enable independent regulation of RGN and sgRNA expression, we constructed separate plasmids for each component. First, the pCAG-mCherry-polyA backbone was generated, which employs the mCherry red fluorescent reporter for tracking transfection and serves as the vector control. Second, the backbone was linearized by digestion with BamHI and HindIII. DNA fragments encoding each RGN were amplified using forward and reverse primers containing homologous arms (forward: CGGAG TCCCAGCAGCCGGATCC$[N]_{20}$; reverse: CGTGGCCGCCGGCCTTTTAC GCGTG$[N]_{20}$, where $[N]_{20}$ denotes gene-specific annealing sequences). The linearized backbone and amplified RGN fragments were assembled via homologous recombination using the Hieff Clone Plus One Step Cloning Kit (10911ES50) to generate CAG promoter-driven constructs (e.g., pCAG-SpCas9-P2A-mCherry-polyA). This strategy yielded expression plasmids encoding 50 engineered RGNs. For sgRNA expression, we used the pCMV-EGFP-polyA-U6-sgRNA backbone, and target-specific spacers were cloned into the U6 promoter-driven cassette. The amino acid sequences of all RGNs, along with the complete sequences of all RGN and sgRNA expression plasmids, are provided in Table S1 (online), with the variable spacer sequences within the sgRNAs indicated as $[N]_{20}$. The specific protospacer sequence corresponding to each RGN is detailed in Table S2 (online).

2.2. Cell culture

HEK293T cells were maintained in DMEM (Yeason, 41401ES) supplemented with 10% fetal bovine serum (FBS, BI, 04-001-1ACS) and 1% penicillin/streptomycin (PS, Beyotime, C0224) at 37 ℃ with 5% CO_2. Cells were passaged at 80%–90% confluence using 0.05% trypsin-EDTA (Yeason, 40127ES80) and seeded into 96-well plates or 100 mm dishes, as needed.

2.3. Cell transfection

Transfections were performed in 96-well plates using polyethylenimine (PEI, Polysciences) when cells reached 40%–50% confluence. Plasmid DNA and PEI (1: 2, *w/w*) were separately diluted in Opti-MEM (Gibco, 31985-070), incubated for 5 min at room temperature, combined, and further incubated for 10 min. The mixture was added dropwise to cells, which were then cultured for 48 h under standard conditions. Double-positive cells ($mCherry^+$ and $EGFP^+$) with fluorescence intensities above 300 were sorted via fluorescence-activated cell sorting (FACS, BD FACSAria III) for downstream analysis (Fig. S1 online).

2.4. Indel efficiency analysis

Genomic DNA was extracted from 1×10^3 sorted cells using 15 μL lysis buffer (50 mmol/L KCl, 1.5 mmol/L $MgCl_2$, 10 mmol/L Tris-HCl, pH 8.5, 0.5% NP40, 0.5% TritonX-100, 10 μg/mL Proteinase K). Target regions were amplified via a nested PCR approach using the Yeasen Hieff® Ultra-Rapid HotStart Master Mix. The target sequences for the three PAM groups (TTTAAN, ATTCCD, and TTGAT) and the corresponding outer and inner primer sequences are provided in Table S3 (online). The inner primers used in the second round of PCR incorporated unique barcodes (Table S3 online) to enable sample multiplexing. Specifically, for each RGN, the 48 corresponding PCR amplicons were pooled into a single library. The pooled products were then purified using a Gel Extraction Kit (Tiangen). Sequencing libraries were constructed by adapter ligation and sequenced on the MGISEQ-T7 platform (MGI). Subsequently, the raw sequencing data were demultiplexed based on the barcode sequences. The demultiplexed reads for each sample were then analyzed using CRISPResso2 (v2.2.8) [45] with the following parameters: a quantification window parameter (-qwc), a minimum alignment score of 50 (-default_min_aln_score), and display of all alleles regardless of frequency (--min_frequency_alleles_around_cut_to_plot 0). Indel frequencies were calculated from the Alleles_frequency_table.zip file.

2.5. Genome-wide, unbiased identification of double-strand breaks (DSBs) enabled by sequencing (GUIDE-seq) analysis

GUIDE-seq experiments were performed as described previously [46]. HEK293T cells were co-transfected with RGN/sgRNA expression plasmids and a blunt, phosphorylated double-stranded oligodeoxynucleotide (dsODN) tag (Table S4 online) using the Lonza 4D-Nucleofector system according to the manufacturer's instructions. Transfected cells were harvested at 72–96 h post-transfection, and genomic DNA was extracted for downstream library construction. Purified genomic DNA was fragmented to 300–700 bp using a Bioruptor Pico (Diagenode) with the following settings: 30 s sonication on, 30 s off, for two cycles. Fragmented DNA was purified using VAHTS DNA Clean Beads (Vazyme,

#N411) and subjected to end-repair, A-tailing, and adapter ligation using a universal DNA library preparation kit (Yeasen, #12197ES24) following the manufacturer's instructions. DNA purification between enzymatic steps was performed using VAHTS DNA Clean Beads (Vazyme, #N411) according to the manufacturer's instructions. Tagged genomic fragments were enriched by two rounds of nested PCR using universal adaptor primers together with primers specific to the dsODN tag (primer sequences listed in Table S4 online). PCR products corresponding to 300–700 bp were purified using a gel extraction kit (TIANgel Purification Kit, DP219) according to the manufacturer's instructions, quantified by Qubit dsDNA HS assay, and sequenced on an Illumina NovaSeq X Plus platform with paired-end 150 bp reads (PE150). Sequencing data were analyzed using the GUIDE-seq pipeline (https://github.com/aryeelab/guideseq). After adapter trimming and quality filtering, dsODN integration sites were mapped to the GRCh38 reference genome. Final off-target sites were identified using the default parameters of the pipeline and merged across biological replicates. For each RGN, three independent biological replicates were performed. mCherry-transfected cells were used as a control, and all insertion sites detected in the mCherry control were excluded from downstream analyses. Only off-target sites with ≤8 mismatches relative to the corresponding sgRNA sequence were retained for final analysis.

2.6. Primer extension-mediated sequencing (PEM-seq) for structural variant detection

PEM-seq in HEK293T cells was performed as described previously [47]. At 72 h post-transfection, approximately 1.5×10^6 transfected cells were sorted and processed for genomic DNA extraction following the original PEM-seq protocol. Cell pellets were gently loosened and resuspended in 500 μL freshly prepared cell lysis master mixture (495 μL cell lysis buffer and 5 μL proteinase K, 20 mg/mL). Samples were incubated at 56 ℃ with shaking at 500 r/min overnight (10–16 h). Genomic DNA was precipitated by the addition of an equal volume of isopropanol, followed by gentle inversion until visible DNA precipitates formed. The DNA pellet was washed by 70% ethanol, and finally dissolved in TE buffer at 56 ℃ with shaking for at least 4 h. DNA concentration and purity were measured by spectrophotometry, and DNA integrity was assessed by agarose gel electrophoresis. Purified genomic DNA (5–10 μg per sample) was fragmented to 300–700 bp using a Covaris S220 ultrasonicator with the following settings: temperature 4 ℃, peak incident power 50 W, duty factor 20%, treatment time 50–65 s, and 200 cycles per burst. Fragmented DNA was subsequently used for PEM-seq library construction. PEM-seq library construction was performed as described previously, comprising the following steps: primer extension with biotin-labeled nucleotides, streptavidin bead capture (Dynabeads™ MyOn™ Streptavidin C1, 65001), on-bead adaptor ligation using T4 DNA ligase (Thermo Scientific, EL0011), and nested PCR amplification (primer sequences in Table S5 online). Final libraries were subjected to size selection by agarose gel electrophoresis. DNA fragments corresponding to 300–700 bp were excised from the gel and purified using a Gel Extraction Kit (TIANgel Purification Kit, DP219) according to the manufacturer's instructions, quantified by Qubit dsDNA HS assay, and sequenced on an Illumina NovaSeq X Plus platform with paired-end 150 bp reads (PE150). Translocation events were analyzed using PEM-Q (https://github.com/liumz93/PEM-Q) by running the built-in PEM-Q.py script with the following parameters: GRCh38 reference genome, cut-site information, chromosome, start and end positions, primer sequences, and strand orientation (positive or negative) (Table S6 online). The resulting Translocation.tab file was filtered to remove sequences containing 4–6 bp tandem repeats occurring four times consecutively, as well as sequences aligning to plasmid sequences.

2.7. Cytotoxicity assessment

Cytotoxicity was assessed using a Cell Counting Kit-8 (CCK-8) assay, following the manufacturer's protocol and as previously described [48]. Sorted cells (5×10^3 cells per well) were seeded into 96-well plates and cultured for 48 h. For each condition, a total of 24 wells were collected after cell sorting. Among these, 18 wells were used for CCK-8-based viability measurements, while the remaining 6 wells were maintained without CCK-8 treatment and used for parallel cell counting. For the CCK-8 assay, culture medium was gently aspirated, and each well was washed twice with PBS to remove residual serum. Subsequently, 10 μL CCK-8 reagent (Sinomol, CCK-810-02) was added to 90 μL fresh medium (FBS and PS free) per well and incubated for 2 h at 37 °C. After incubation, 90 μL of supernatant from each well was transferred to a new 96-well plate, and absorbance at 450 nm was measured using a microplate reader (Tecan Spark). Each assay plate included medium-only wells as blank controls. For data analysis, every six CCK-8-treated wells were averaged to generate one biological replicate, resulting in three independent replicates per condition. The remaining six untreated wells were subjected to direct cell counting using an automated cell counter (RWD, C100-SE) to provide an independent assessment of cytotoxicity.

2.8. RNA isolation and RNA-seq

At 48 h post-transfection, transfected cells were sorted (200,000 cells per sample), and total RNA was extracted using Trizol (Ambion) following the manufacturer's protocol. High-throughput mRNA sequencing was performed on the MGISEQ-T7 platform (MGI). RNA-seq analysis was conducted using DESeq (v1.46.0), with differentially expressed genes defined by the criteria (absolute $\log_2$-transformed fold-change >1 and P-value <0.05). GO enrichment analysis was performed using clusterProfiler (v4.14.6).

2.9. Bioinformatics

Raw sequencing data were demultiplexed (fastq-multx v1.4.2), quality-checked (FastQC v0.11.8), and trimmed (Trimmomatic v0.39). Reads were aligned to the GRCh38 reference genome using STAR (v2.7.10a) with a two-pass strategy. Figures were generated using ggplot2 (v3.4.2) and pheatmap (v1.0.12) in R (v4.5.1).

3. Results

3.1. Comparative editing efficiency across 50 RGNs at multiple endogenous sites

To evaluate the editing efficiency of RGNs across multiple endogenous sites, we selected 50 extensively studied RGNs that characteristically target a 5' PAM. Drawing upon previous studies, we adopted the PAM sequences and sgRNA lengths for each RGN [7,8,10,13,26–46]. Given the variability in PAM requirements, our analysis concentrated on three widely used PAM types: TTAAN, ATTCCD, and TTGAT (Fig. 1a).

To ensure a fair comparison, we screened the GRCh38 reference genome for endogenous target sites with 5'-PAM-$(N)_{21}$GG sequences. RGNs with the same PAM type were assigned identical guide sequences to minimize variability in chromatin accessibility and epigenetic factors. These target sites also included a 3'-NGG-PAM compatible with SpCas9. Using SpCas9 as a reference control,

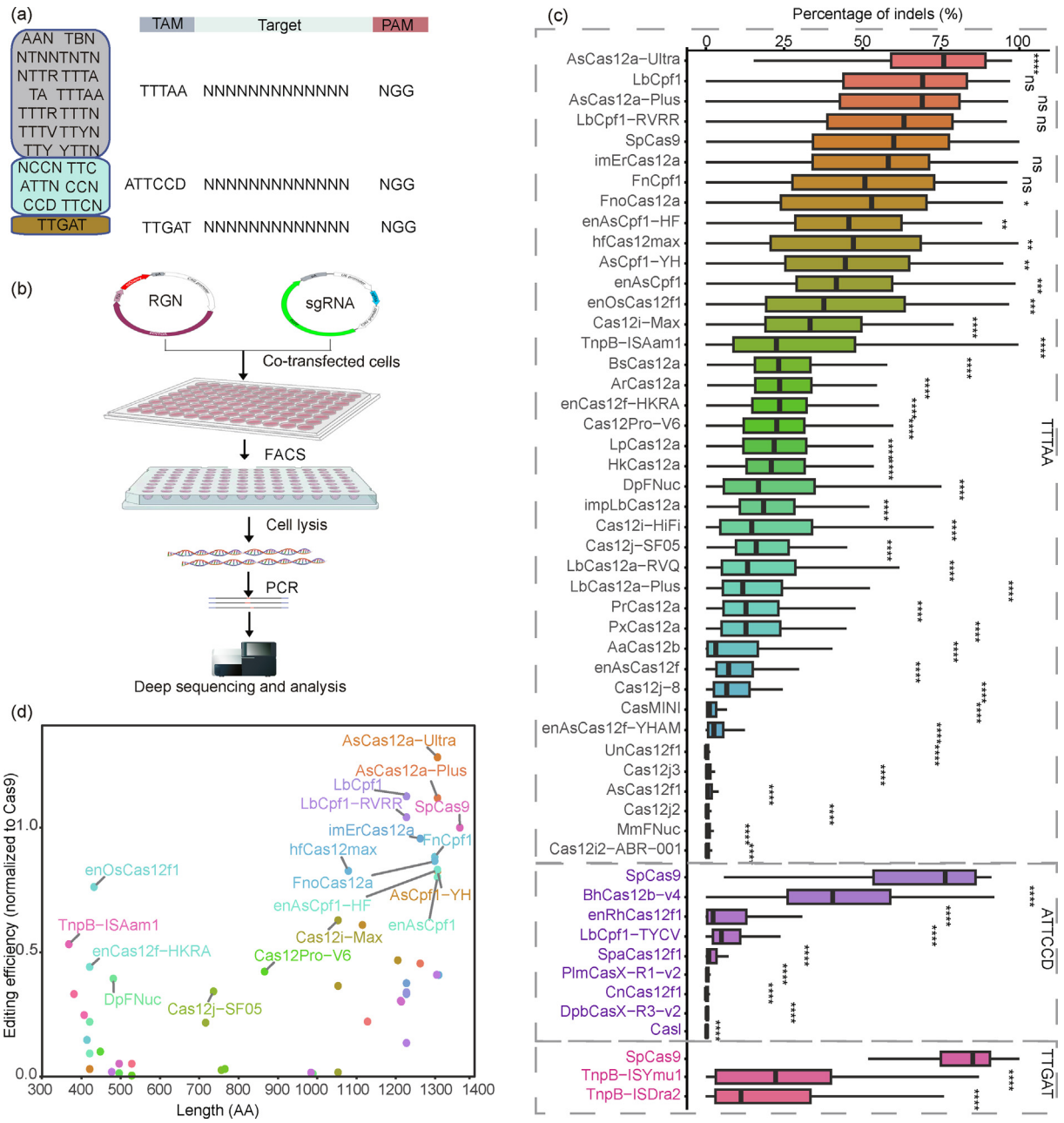


Fig. 1. Editing efficiencies of 50 RGNs at endogenous target sites. (a) PAM classification of RGN. PAM sequences from 50 RGNs were categorized into three classes: TTAAN, ATTCCD, and TTGAT. All constructs included a 3′-terminal NGG PAM (SpCas9-compatible control). Representative PAM motifs and structural features are listed. TAM, the target-adjacent motif, is analogous to the PAM but is specifically referred to as such in ωRNA systems that are independent of the CRISPR machinery [49]. (b) Experimental workflow. HEK293T cells were co-transfected with red fluorescent protein (mCherry)-tagged RGN plasmids and green fluorescent protein (EGFP)-tagged sgRNA plasmids. Dual-positive cells were sorted by FACS 48 h post-transfection. Genomic DNA was amplified by PCR, sequenced, and analyzed to quantify editing efficiencies. (c) Editing efficiency of 50 RGNs. Box plots showing indel frequencies of RGNs grouped by PAM class (TTAAN, ATTCCD, TTGAT, top to bottom). The SpCas9 served as the control. Boxes represent the 25th, 50th (median), and 75th percentiles. Statistical significance was determined by one-way ANOVA analysis using SpCas9 as the control. $P < 0.05$ was considered significant. ns: not significant; $^{*}P < 0.05$; $^{**}P < 0.01$; $^{***}P < 0.001$; $^{****}P < 0.0001$. (d) Normalized editing efficiency versus RGN length. Using SpCas9 as the reference. Editing efficiencies are plotted against RGN protein length (AA). Displaying the names of 19 RGNs with relatively high editing efficiency.

we compared their editing efficiencies and extensively characterized their properties and general applicability. Using a custom script for sgRNA identification, we identified approximately 40,000 target sites in the GRCh38 reference genome. After filtering out lethal gene sites, repetitive sequence sites, and sites on the X and Y chromosomes, around 4000 sites remained. From this set, 48 sites were randomly selected for each PAM type for targeting in experimental analysis.

The RGNs and their respective sgRNAs were expressed from two separate plasmids co-transfected into HEK293T cells, one expressing the RGN-P2A-mCherry and the other expressing the sgRNA along with EGFP. At 48 h post-transfection, double-positive cells expressing both red and green fluorescent markers were isolated by FACS. These cells were then lysed, and the target regions were amplified from gDNA by PCR (Fig. 1b).

High-throughput sequencing analysis demonstrated excellent reproducibility between replicates, as evidenced by a strong Pearson correlation ($R^2 = 0.85$, $P < 0.0001$) (Fig. S2a online). RGNs targeting the TTAAN PAM, including AsCas12a-Ultra (69.84%), LbCpf1 (61.30%), AsCas12a-Plus (60.93%) and LbCpf1-RVRR

(56.73%), exhibited higher editing efficiency compared to SpCas9 (54.45%), although only AsCas12a-Ultra showed a statistically significant increase (one-way ANOVA, $P < 0.0001$ versus SpCas9) (Fig. 1c, Fig. S2b online). In contrast, all RGNs within the ATTCCD and TTGAT PAM groups showed lower cleavage activity than SpCas9, with BhCas12b-v4 exhibiting relatively higher activity than others (Fig. 1c, Table S7 online). In general, RGNs with higher editing efficiencies tended to be larger (>1000 AA), except enOsCas12f1, a compact RGN comprising only 432 AA, which achieved a noteworthy editing efficiency of 41.50% (Fig. 1d, Fig. S3 online).

3.2. Characteristics of edited products at endogenous sites

The 13 top-performing RGNs (editing efficiency ≥70% of SpCas9 activity) selected for subsequent analysis of their editing properties included AsCas12a-Ultra (69.84%), LbCpf1 (61.30%), AsCas12a-Plus (60.93%), LbCpf1-RVRR (56.73%), SpCas9 (54.45%), imErCas12a (52.06%), FnCpf1 (48.05%), FnoCas12a (47.18%), enAsCpf1-HF (45.30%), hfCas12max (45.02%), AsCpf1-YH (45.01%), enAsCpf1 (43.64%) and enOsCas12f1 (41.50%) (Fig. 1c). To increase RGN diversity in our comparison, we also selected six additional RGNs from distinct families with relatively high efficiencies, including Cas12i-Max (34.22%), TnpB-ISAam1 (28.98%), enCas12f-HKRA (24.02%), Cas12Pro-V6 (23.00%), DpFNuc (21.45%), and Cas12j-SF05 (18.67%) (Fig. 1c). Examination of deletion patterns at endogenous sites for these 19 RGNs showed that deletion probabilities generally increased from upstream positions (1–10), peaked at mid-segment positions (15–25), and gradually declined beyond position 25 for most RGNs (beginning at the 5' end of the target sequence, with the first base as position 1) (Fig. 2a).

Further analysis of the primary deletion range (i.e., the peak position and regions within 70% of the peak value) highlighted differences among the RGNs. Specifically, SpCas9, FnCpf1, and FnoCas12a predominantly induced a high density of deletions at base pairs 18–21. In contrast, Cas12i-Max exhibited a broader deletion range (positions 17–26). Notably, enOsCas12f1 exhibited a unique deletion pattern, with a peak at position 24 and deletions predominantly occurring downstream of the target sequence (positions 20–26) (Fig. 2a).

Additionally, analysis of deletion lengths revealed distinct differences among the RGNs (Fig. 2b, Fig. S4a, b online). SpCas9 and TnpB-ISAam1 primarily induced short deletions of 1–2 bp, with the highest proportions observed for this category (58.33% and 52.07%, respectively), showing no significant difference in detection ratio between them (one-way ANOVA, $P < 0.05$). In contrast, other tested RGNs exhibited significantly lower 1–2 bp deletion ratios compared to SpCas9 ($P < 0.05$), excluding Cas12Pro-V6. The majority of other RGNs predominantly generated deletions ranging from 3–10 bp, with proportions exceeding 30%. Among these, AsCas12a-Ultra yielded the highest proportion of 3–10 bp deletions (54.93%). Notably, Cas12i-Max was exceptional in predominantly generating long deletions exceeding 10 bp (29.53%). Furthermore, Cas12Pro-V6, Cas12i-Max, and enAsCpf1 all showed significantly higher proportions of these long deletions (>10 bp) compared to SpCas9 ($P < 0.0001$).

3.3. Analysis of sgRNA-dependent off-target effects of 19 RGNs

We then compared them by GUIDE-seq experiments [46]. RGN off-target sites with eight or fewer mismatches from the intended target sequence were retained [46]. Quantification of sgRNA-dependent off-target activity revealed strikingly different sgRNA-dependent off-target effects of the 19 RGNs across the genome using GUIDE-seq, enabling inferences in specificity based on the number of off-target sites detected (defined as dsODN-integrated loci). Among them, DpFNuc displayed the highest propensity for introducing off-target counts (mean 541 sites), followed by enCas12f-HKRA (168 sites), and Cas12i-Max (153 sites). However, only DpFNuc showed a statistically significant increase in off-target counts compared to SpCas9 ($P < 0.01$) (Fig. 3a, Table S7 online). In contrast, AsCpf1-YH exhibited the lowest off-target activity (99 sites), outperforming even SpCas9 (120 sites), while RGNs, such as FnCpf1 (114 sites) and Cas12j-SF05 (127 sites), showed intermediate off-target risks (Fig. 3a, Table S7 online). To validate the GUIDE-seq detection, we selected three representative RGNs spanning the spectrum of off-target activity: DpFNuc (highest off-target), SpCas9 (medium), and AsCpf1-YH (lowest). We designed specific primers targeting the top 16 detected off-target sites (ranked by abundance) for each RGN and performed deep targeted amplicon sequencing using genomic DNA extracted from both RGN/sgRNA-treated cells. This orthogonal validation confirmed significant indel frequencies at 16/16 (100%) sites for DpFNuc, 15/16 (93.8%) for SpCas9, and 16/16 (100%) for AsCpf1-YH (Fig. S5a online).

Furthermore, editing efficiency of 19 RGNs showed a negligible correlation with sgRNA-dependent off-target activity ($R^2 = 0.13$, $P = 0.125$) (Fig. S5b online). Subsequent examination of the chromosomal distribution of off-target sites across the 19 RGNs identified significant enrichment at several specific genomic regions (Fig. 3b, Fig. S5c online). For example, targeting the sg16 site resulted in clusters of off-target hotspots in two genomic regions (chr1: 125,174,000–125,181,599 and chr1: 143,185,250–143,264,549) (Fig. 3b). Genome-wide annotation revealed that off-target sites were predominantly located in introns (57.45%), followed by intergenic regions (33.04%) and exons (9.51%) (Fig. 3c). Although the low proportion of exonic off-target events might limit direct disruption of coding sequences (CDS), RGNs in intergenic and intronic regions could still indirectly impair cellular functions by interfering with regulatory elements.

3.4. Genomic structural changes associated with RGNs

To compare genomic structural changes among the 19 RGNs, we conducted PEM-seq analysis [47] to detect chromosomal translocations resulting from off-target activity, using biotin-labeled primers upstream of DSBs to capture sequences downstream of the DSBs that are ligated during DNA repair (Fig. 4a).

Pearson correlation analysis revealed that chromosomal translocation frequency was significantly positively correlated with overall editing activity ($R^2 = 0.53$, $P < 0.01$) (Fig. S6a online). Further analysis distinguished sgRNA-dependent (with translocation sequence similarity to the target site) and sgRNA-independent (without such similarity) translocation events across the 19 RGNs. In general, sgRNA-dependent translocations exhibited low percentages (3.77%–31.63%), with DpFNuc (31.63%) and enCas12f-HKRA (20.09%) showing markedly higher rates than other RGNs (Fig. 4b). While sgRNA-independent translocations were more closely associated with editing activity ($R^2 = 0.518$, $P < 0.001$) (Fig. S6b online), sgRNA-dependent translocations showed no strong correlation with RGN editing activity ($R^2 = 0.299$, $P < 0.05$) (Fig. S6c online). Moreover, GUIDE-seq detected off-target sites shared a strong positive correlation with PEM-seq quantified sgRNA-dependent translocation frequencies ($R^2 = 0.71$, $P < 0.001$) (Fig. S6d online). Therefore, sgRNA-dependent translocation serves as a better indicator of RGN-associated translocation risk. Comparative analysis of chromosomal translocation rates among RGNs indicated that enCas12f-HKRA (1.56%), hfCas12max (1.49%), and imErCas12a (1.03%) exhibited the highest translocation rates, while SpCas9 (0.78%), enAsCpf1 (0.75%), and AsCpf1-YH (0.74%) displayed relatively moderate rates. Alternatively, FnoCas12a (0.44%), enOsCas12f1

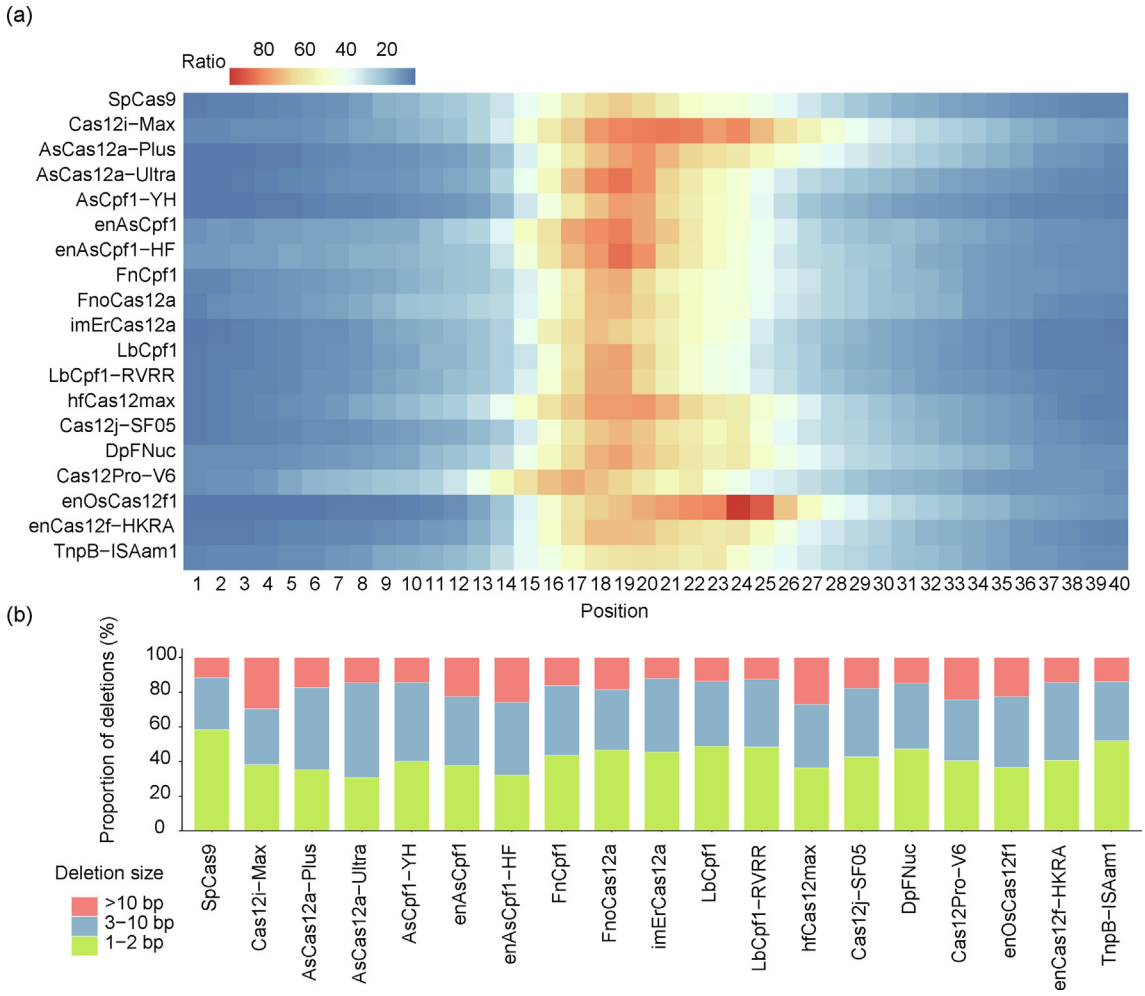


Fig. 2. Deletion patterns induced by representative RGNs. (a) Deletion initiation sites. Heatmap visualization of the percentage of total deletion events initiating at each nucleotide position (position 1: first base of target sequence), with color intensity increasing from blue to red for each representative RGN. (b) Distribution of 19 representative RGNs according to deletion length. Proportions of deletions are grouped as 1–2 bp (green), 3–10 bp (blue), and >10 bp (red).

(0.40%), and Cas12j-SF05 (0.01%) showed the lowest translocation rates (Fig. 4c, Table S7 online).

Analysis of chromosomal distribution of translocation hotspots revealed that 49.33% (37/75) translocation events detected across all RGNs were clustered near target site 16 (chr17: 1,486,158), while additional hotspots were identified on chr1 (8/75), chr16 (6/75), chr19 (5/75), and chr21 (9/75) (Fig. 4d). Genomic annotation analysis showed that translocation sites were predominantly located in introns (57.36%), followed by intergenic regions (28.97%), and exons (13.67%) (Fig. S6e online).

3.5. Analysis of cytotoxicity associated with the 50 RGNs

Following editing efficiency and genotoxicity assessment, we next examined RGN cytotoxicity in HEK293T cells. For all 50 RGNs, cytotoxicity was comprehensively evaluated through CCK-8 assay and direct cell counting to assess proliferation. Pearson correlation analysis confirmed that the CCK-8 assay results were highly reproducible among technical replicates (R^2 = 0.90, P < 0.001) (Fig. S7a online). Notably, the results of both assays were strongly correlated across all RGNs (R^2 = 0.58, P < 0.001, Fig. S6b online). Using SpCas9 as the reference standard, untreated wild-type (WT) cells displayed the highest viability, with normalized values of 2.38 (CCK-8 assay) and 3.06 (direct cell counting), both standardized to a baseline of 1 for comparative analysis (Fig. S7b online). Among RGNs, enRhCas12f1 (CCK-8 = 1.29), SpaCas12f1 (1.24), and HkCas12a (1.16) exhibited the highest normalized CCK-8 values, surpassing that of SpCas9 (CCK-8 = 1.00), indicating minimal cytotoxicity. In contrast, Cas12i-HiFi (CCK-8 = 0.48) and enAsCpf1-HF (CCK-8 = 0.45) showed the highest cytotoxic effects. TnpB-ISAam1 treatment also led to markedly reduced cell viability (0.66) (Fig. 5a, Table S7 online).

To explore the potential molecular mechanisms underlying the observed cytotoxicity, Gene Ontology (GO) analysis was conducted on the RNA-seq data from each RGN. This revealed significant enrichment in pathways such as response to virus, negative regulation of viral genome replication, cellular response to type I interferon, and response to type I interferon (Fig. S7c online). By integrating RNA-seq data with CCK-8 results, and using SpCas9 RNA-seq data as a reference, we observed that RGNs in the high-cytotoxicity group significantly affected the expression of genes related to ribosomal function and mitochondrial respiratory chain activity, which could strongly impact overall cell viability (Fig. 5b). Analysis of differentially expressed genes revealed significant downregulation ($|\log_2$ fold change$|$ < 1) of ribosomal subunit genes such as *RPS27A*, *RPL35A* and *RPL26* (Fig. S8a online), suggesting impaired ribosome biogenesis. Functional enrichment analysis showed that pathways such as structural constituent of ribosome and cytosolic ribosome were enriched in the high-cytotoxicity group (q < 0.05, Fig. 5b). Additionally, key mitochondrial respira-

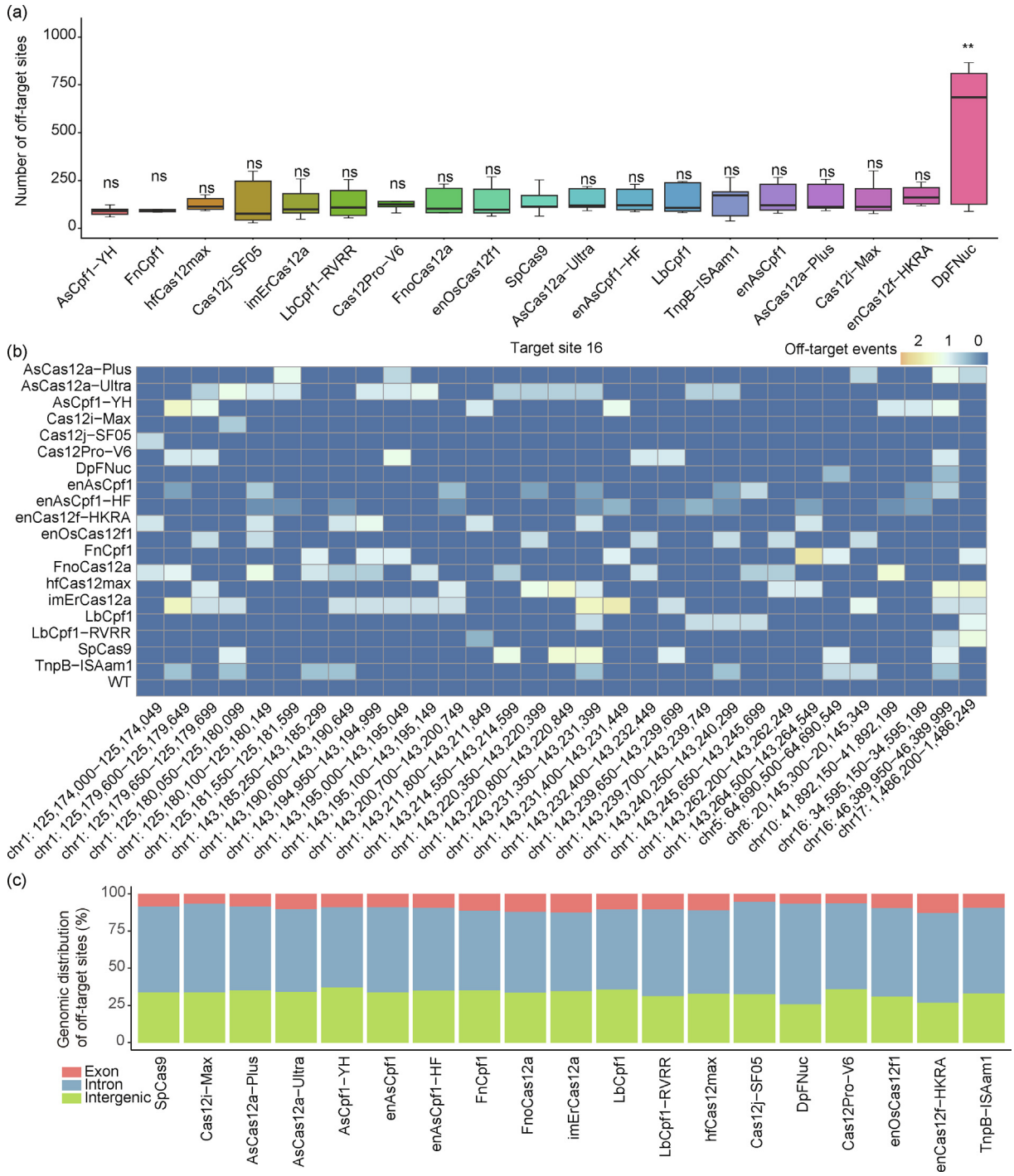


Fig. 3. GUIDE-seq analysis of sgRNA-dependent off-targets. (a) Number of off-target sites. Box plots of sgRNA-dependent off-target sites detected by GUIDE-seq for the 19 RGNs. For each RGN, three independent biological replicates were performed per target site (sites 10, 16, and 44). Boxes represent the 25th, 50th (median), and 75th percentiles. Statistical significance was determined by one-way ANOVA analysis using SpCas9 as the control. $P < 0.05$ was considered significant. ns: not significant; $^{**}P < 0.01$. (b) Chromosomal distribution near target site 16. Heatmap highlighting off-target hotspot regions detected by GUIDE-seq. Each point represents a 50 bp genomic window, with regions designated as hotspots if they contain off-target events from at least three distinct RGNs, with color intensity increasing from blue to red for each representative RGN. (c) Genomic annotation of off-target sites. Bar plots illustrating the distribution of off-target sites across intronic, exonic, and intergenic regions for the 19 RGNs. Red: Exon, blue: Intronic, green: Intergenic.

tory chain genes, including *NDUFS4*, *NDUFB6*, *COX5B*, and *UQCRQ*, were downregulated (Fig. S8b online).

4. Discussion and conclusion

In this study, we systematically evaluated the editing efficiency, off-target effects, and cytotoxicity of RGNs, providing a valuable reference to guide the selection of gene-editing tools for current applications. These findings establish fundamental criteria for the future discovery of novel genome editors and the rational optimization of existing systems. Our results underscore the diversity of RGN activity, targeting specificity, genomic stability, and impacts on cellular functions. To assess their overall performance in detail, we established a multidimensional evaluation framework integrating cytotoxicity (1-normalized CCK-8 value), genotoxicity

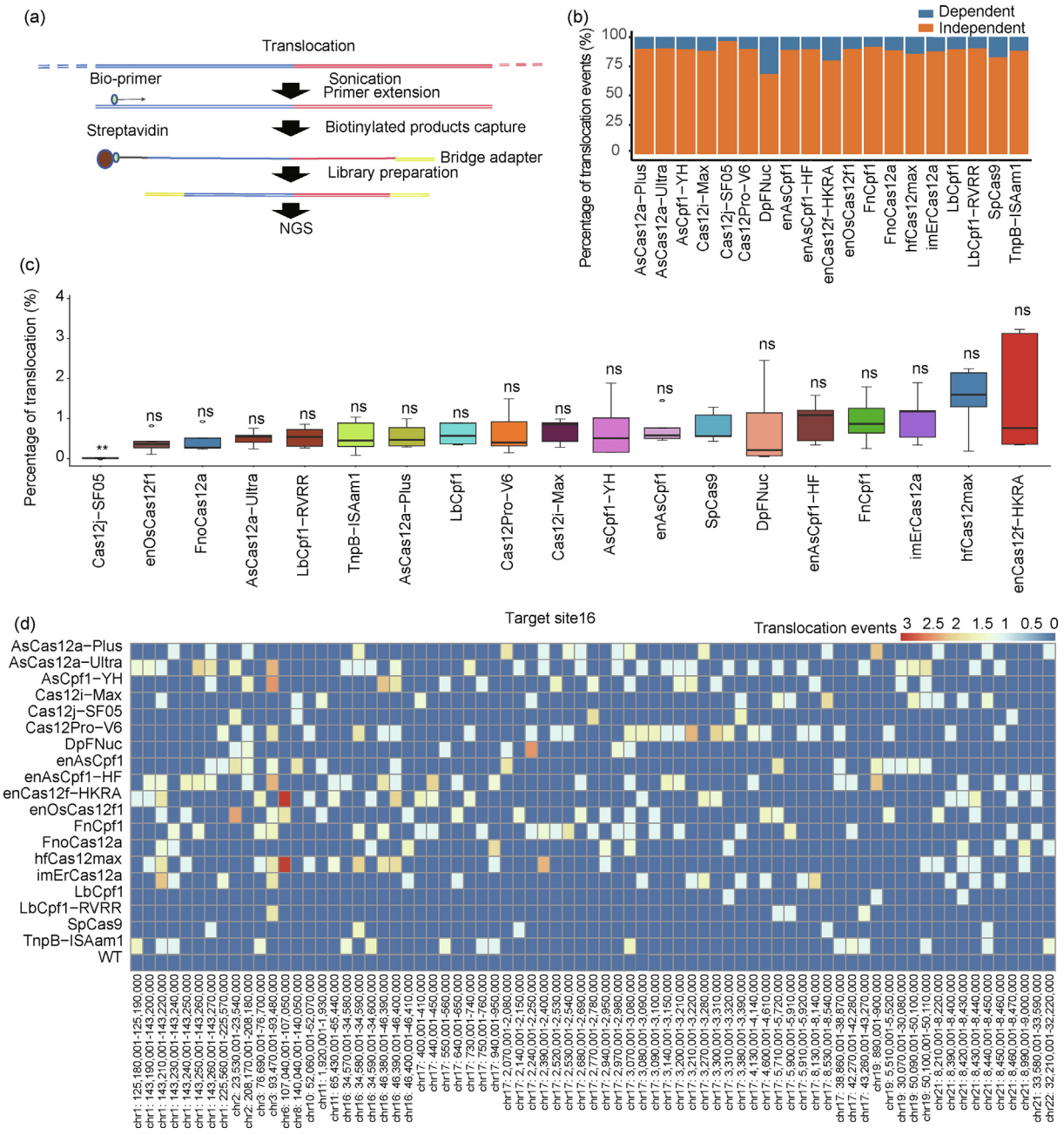


Fig. 4. Structural variant profiling by PEM-seq. (a) PEM-seq workflow. Cells were lysed, sonicated, and processed for primer extension, adaptor ligation, and sequencing to detect chromosomal translocations. (b) Sequence similarity of translocation breakpoints. Bar graphs showing the percentage of breakpoints with (sgRNA-dependent) or without (sgRNA-independent) sequence similarity to the on-target site. (c) sgRNA-dependent translocation frequencies at three loci. Box plots showing sgRNA-dependent translocation rates across genomic sites detected by PEM-seq for 19 representative RGNs. For each RGN, translocation efficiencies measured at the three loci were averaged to calculate the final translocation frequency. Boxes represent the 25th, 50th (median), and 75th percentiles. Statistical significance was determined by one-way ANOVA analysis using SpCas9 as the control. $P < 0.05$ was considered significant. ns: not significant; $^{*}P < 0.05$; $^{**}P < 0.01$. (d) Translocation hotspots at target site 16. Heatmap of breakpoint clusters (≥3 events per region) mapped to chromosomal coordinates. Each point represents a 10,000 bp genomic window, and only regions with off-target events from at least three different RGNs are designated as hotspots.

(the product of GUIDE-seq off-target sites and PEM-seq translocation frequencies), and editing activity (normalized to SpCas9). Simultaneous visualization of these properties in three dimensions reveals distinct trade-offs between efficiency and specificity among different RGNs (Fig. 6, Table S7 online).

In practical applications, we tend to prioritize RGNs that exhibit high cleavage activity, low genotoxicity, and minimal cytotoxicity. However, parallel comparisons revealed that several high-activity RGNs, such as AsCas12a-Ultra, LbCpf1, and AsCas12a-Plus, demonstrated higher editing efficiency than SpCas9 but were often accompanied by increased genomic disturbances, such as significantly elevated chromosomal translocation rates (Fig. S6a online). This phenomenon may be mechanistically related to the spatial proximity between DSB sites and fragile genomic regions. When active editing sites are physically close to translocation-prone loci, concurrent DSBs are more likely to trigger erroneous repair via non-homologous end joining (NHEJ), leading to chromosomal rearrangements [50]. This spatial dependency underscores the importance of considering three-dimensional chromatin structure when selecting target sites for therapeutic purposes, especially in applications where minimizing structural variants is critical.

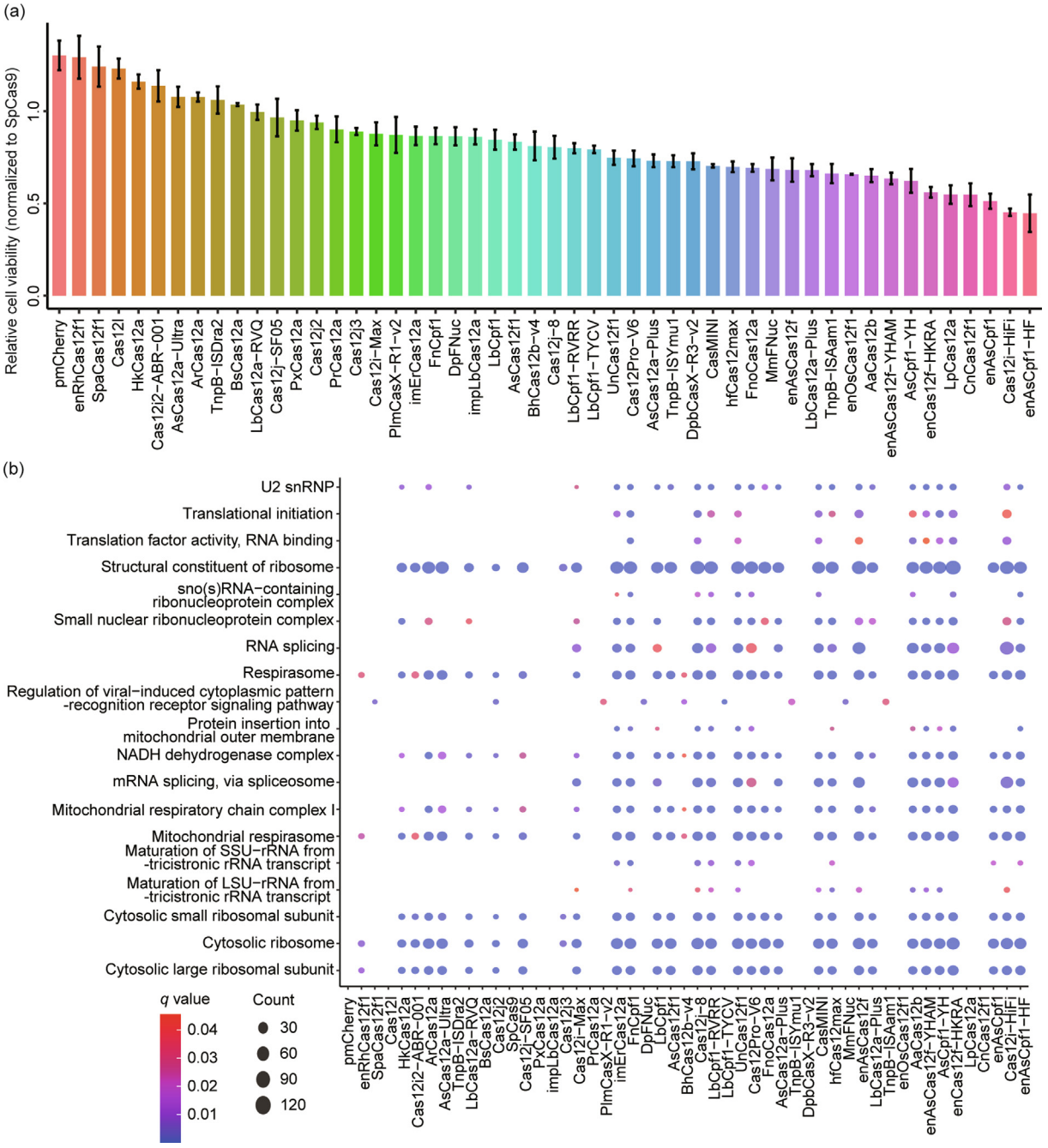


Fig. 5. Cytotoxicity and transcriptomic impacts of 50 RGNs. (a) Cell viability assays. CCK-8 assays (normalized to SpCas9) of HEK293T cells expressing each respective RGN. (b) GO term functional enrichment analysis of genes disrupted by each RGN. Enriched GO terms from RNA-seq analysis for 50 RGNs. Bubble size represents gene count enriched in each GO term, and the color indicates the adjusted Pearson value, with color intensity increasing from blue to red for each representative GO term.

In addition, our analysis found no significant statistical correlation between off-target frequency and editing efficiency, suggesting that these properties may be mechanistically decoupled, likely reflecting distinct biophysical constraints in interaction between enzymatic activity and targeting specificity [51]. This orthogonal relationship suggests that optimization of activity and specificity can proceed independently, enabling the engineering of editors with simultaneous high efficiency and precision. The off-target effects quantified from PEM-seq analysis also highlighted notable differences in RGN specificity. Among these, AsCpf1-YH and FnCpf1 exhibited relatively low sgRNA-dependent off-target risks, indicating their potential as reliable tools for precision applications. In contrast, DpFNuc showed a high number of off-target sites (541 on average) but a relatively low chromosomal translocation rate (0.52%), likely due to its low overall cleavage activity, which limits DSBs formation.

For *in vivo* therapeutic applications, the molecular dimensions of RGNs emerge as a critical selection parameter. Notably, compact variants like enOsCas12f1 (432 AA) demonstrate superior compatibility with AAV delivery systems due to their minimal genomic payload requirements [11]. EnOsCas12f1 also exhibits relatively high editing activity and low genotoxicity, making it particularly advantageous for *in vivo* gene therapy, especially in the context of neurological disorders [52].

In terms of cytotoxicity, different RGNs showed substantial performance variability. Notably, AsCas12a-Ultra achieved the highest editing activity (69.84%) while exhibiting extremely low cytotoxicity (CCK-8 = 1.08), making it a promising candidate for gene edit-

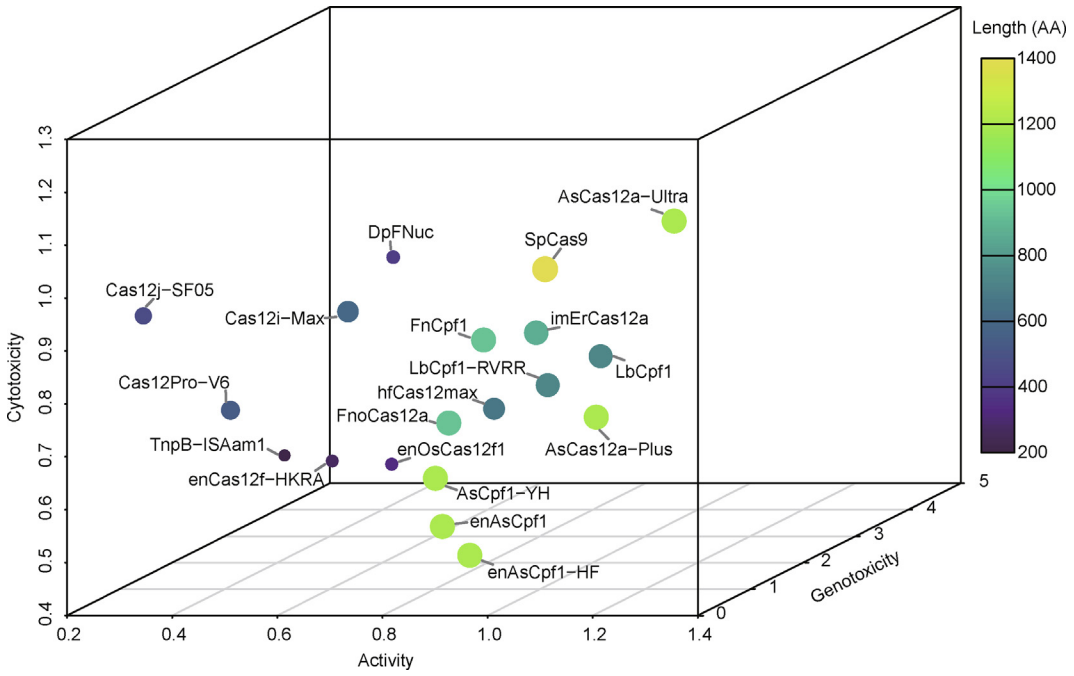


Fig. 6. Multidimensional profiling of RGN performance. Cytotoxicity (normalized CCK-8 value), genotoxicity (the product of the normalized number of GUIDE-seq off-target sites and normalized PEM-seq translocation frequencies), and normalized editing activity are plotted in three dimensions for 50 RGNs. RGN size (amino acid length) is represented by a color gradient ranging from 200 to 1400 AA, with color intensity increasing from blue to green for each representative RGN.

ing in sensitive or rare cell types such as primary cells or stem cells. Comparably, enAsCpf1-HF, despite reaching a higher editing efficiency of 45.30%, severely inhibited cell proliferation (CCK-8 = 0.45), significantly limiting its clinical applicability. The observed cytotoxicity of RGNs may be linked to their impact on essential cellular processes. Transcriptomic analysis revealed consistent downregulation of ribosome-associated genes (e.g., *RPS27A* and *RPL35A*) and mitochondrial respiratory chain genes (e.g., *NDUFS4* and *COX5B*) in highly cytotoxic RGNs. This may be attributable to unintended RNase activity inherent in certain RGNs, which could degrade cellular RNAs, including rRNA and mRNAs encoding components of oxidative phosphorylation, thereby disrupting ribosome biogenesis and ATP production [20,53,54]. This cascade of molecular events ultimately results in reduced metabolic activity and proliferation arrest, as observed in the CCK-8 assays (Fig. 5a). These findings further highlight the need to strike a careful balance among editing efficiency, targeting specificity, delivery feasibility, and cytotoxicity when designing genome editors.

Our systematic quantification of these key performance metrics establishes both an immediately applicable dataset for rational RGN selection in current applications and an analytical framework for evaluating efficiency-specificity trade-offs, thereby identifying precise molecular targets for engineering enhanced genome editing systems. However, several limitations of this study should be acknowledged. First, our analysis was primarily based on the broad PAM sequences reported for each RGN to enable parallel comparison across identical genomic loci, which may not reflect their activity under optimally refined PAM conditions. Second, all experiments were conducted in HEK293T cells, which may not fully represent editing outcomes in primary cells or *in vivo* systems. Third, the observed higher editing efficiency of four Cas12a variants (AsCas12a-Ultra, LbCpf1, AsCas12a-Plus, and LbCpf1-RVRR) compared to SpCas9 may partially stem from site-specific biases in our experimental design. While these results challenge prior reports suggesting SpCas9's superior activity, discrepancies could arise from differences in target site selection, chromatin accessibility, or epigenetic contexts across studies [15,19,53]. Finally, it should be noted that our efficiency measurements relied on FACS-based enrichment of transfected cells, a method optimized for comparative screening to minimize noise from variable transfection efficiency, but one that is distinct from unselected delivery contexts *in vivo*. This approach is well-established in prior comparative studies [55]. The editing efficiencies reported here should therefore be interpreted as the intrinsic activity within successfully transfected cells, rather than the editing rates in bulk cell populations or in therapeutic settings without selection. Moreover, our assessment framework in this study is adaptable to new research-specific parameters, such as tissue-specific delivery efficiency or epigenetic context, thus expanding its utility for precision genome engineering. Future development efforts will also focus on optimizing RGNs to balance efficiency and specificity, while elucidating their direct effects on cellular pathways. By integrating molecular size, delivery constraints, and functional trade-offs, this multidimensional approach provides a data-driven roadmap for tailoring genome-editing tools to specific experimental or therapeutic goals.

Conflict of interest

The authors declare that they have no conflict of interest.

Acknowledgements

This work was supported by Shenzhen Medical Research Fund (B2502040), the National Natural Science Foundation of China (32371549), Seed Industry Vitalization Program of Jiangsu Province (JBGS[2021]025), the Agricultural Science and Technology Innovation Program (ASTIP) (Y2024QC32, CAAS-CSIAF-202401, CAAS-BRC-AFIS-2025-03, and CAAS-SCAB-202301). We thank all the colleagues in the Zuo lab for their technical assistance and helpful discussions. The graphical abstract and Fig. 1b incorporate several materials provided by DBCLS (Database Center for Life

Science), available at https://togotv.dbcls.jp/en/pics.html. These materials are used under the terms of the Creative Commons Attribution 4.0 International License (https://creativecommons.org/licenses/by/4.0/). Modifications have been made to the original materials.

Author contributions

Erwei Zuo, Dali Li, Haoyi Wang, Jiazhi Hu, Jitan Zheng, and Hu Feng designed the study. Hu Feng, Erwei Zuo, and Mingdi Wu performed data analysis. Jitan Zheng, Xueyan Wang, and Jing Liu performed the experiments. Erwei Zuo supervised the project. Jitan Zheng, Mingdi Wu and Erwei Zuo wrote the paper.

Data availability

The raw data were deposited in the National Center for Biotechnology Information (NCBI) Sequence Read Archive database under accession PRJNA1103429.

Appendix A. Supplementary material

Supplementary data to this article can be found online at https://doi.org/10.1016/j.scib.2026.03.047.

References

[1] Barrangou R, Fremaux C, Deveau H, et al. CRISPR provides acquired resistance against viruses in prokaryotes. Science 2007;315:1709–12.
[2] Jinek M, Chylinski K, Fonfara I, et al. A programmable dual-RNA-guided DNA endonuclease in adaptive bacterial immunity. Science 2012;337:816–21.
[3] Cong L, Ran FA, Cox D, et al. Multiplex genome engineering using CRISPR/Cas systems. Science 2013;339:819–23.
[4] Lettre G, Bauer DE. Fetal haemoglobin in sickle-cell disease: from genetic epidemiology to new therapeutic strategies. Lancet 2016;387:2554–64.
[5] Wu Y, Zeng J, Roscoe BP, et al. Highly efficient therapeutic gene editing of human hematopoietic stem cells. Nat Med 2019;25:776–83.
[6] Hsu PD, Lander ES, Zhang F. Development and applications of CRISPR-Cas9 for genome engineering. Cell 2014;157:1262–78.
[7] Zetsche B, Gootenberg JS, Abudayyeh OO, et al. Cpf1 is a single RNA-guided endonuclease of a class 2 CRISPR-Cas system. Cell 2015;163:759–71.
[8] Karvelis T, Druteika G, Bigelyte G, et al. Transposon-associated TnpB is a programmable RNA-guided DNA endonuclease. Nature 2021;599:692–6.
[9] Schilling C, Koffas MAG, Sieber V, et al. Novel prokaryotic CRISPR-Cas12a-based tool for programmable transcriptional activation and repression. ACS Synth Biol 2020;9:3353–63.
[10] Wu Z, Zhang Y, Yu H, et al. Programmed genome editing by a miniature CRISPR-Cas12f nuclease. Nat Chem Biol 2021;17:1132–8.
[11] Chew WL, Tabebordbar M, Cheng JK, et al. A multifunctional AAV-CRISPR-Cas9 and its host response. Nat Methods 2016;13:868–74.
[12] Yoon PH, Skopintsev P, Shi H, et al. Eukaryotic RNA-guided endonucleases evolved from a unique clade of bacterial enzymes. Nucleic Acids Res 2023;51:12414–27.
[13] Saito M, Xu P, Faure G, et al. Fanzor is a eukaryotic programmable RNA-guided endonuclease. Nature 2023;620:660–8.
[14] Schmid-Burgk JL, Gao L, Li D, et al. Highly parallel profiling of Cas9 variant specificity. Mol Cell 2020;78:794–800.
[15] Xin C, Yin J, Yuan S, et al. Comprehensive assessment of miniature CRISPR-Cas12f nucleases for gene disruption. Nat Commun 2022;13:5623.
[16] Seo S-Y, Min S, Lee S, et al. Massively parallel evaluation and computational prediction of the activities and specificities of 17 small Cas9s. Nat Methods 2023;20:999–1009.
[17] Fiumara M, Ferrari S, Omer-Javed A, et al. Genotoxic effects of base and prime editing in human hematopoietic stem cells. Nat Biotechnol 2023;42:877–91.
[18] Huang H, Huang G, Tan Z, et al. Engineered Cas12a-plus nuclease enables gene editing with enhanced activity and specificity. BMC Biol 2022;20:91.
[19] Zhang L, Zuris JA, Viswanathan R, et al. AsCas12a ultra nuclease facilitates the rapid generation of therapeutic cell medicines. Nat Commun 2021;12:3908.
[20] Kleinstiver BP, Sousa AA, Walton RT, et al. Engineered CRISPR-Cas12a variants with increased activities and improved targeting ranges for gene, epigenetic and base editing. Nat Biotechnol 2019;37:276–82.
[21] Welker E, Tálas A, Ligeti Z, et al. Improved lbCas12a variants with altered pam specificities further broaden the genome targeting range of Cas12a nucleases. Nucleic Acids Res 2020;48:3722–33.
[22] Wierson WA, Simone BW, WareJonCas Z, et al. Expanding the CRISPR toolbox with ErCas12a in zebrafish and human cells. CRISPRJ 2019;2:417–33.
[23] Liu P, Luk K, Shin M, et al. Enhanced Cas12a editing in mammalian cells and zebrafish. Nucleic Acids Res 2019;47:4169–80.
[24] Zhang L, Li G, Zhang Y, et al. Boosting genome editing efficiency in human cells and plants with novel lbCas12a variants. Genome Biol 2023;24:102.
[25] Strecker J, Jones S, Koopal B, et al. Engineering of CRISPR-Cas12b for human genome editing. Nat Commun 2019;10:212.
[26] Teng F, Cui T, Feng G, et al. Repurposing CRISPR-Cas12b for mammalian genome engineering. Cell Discov 2018;4:63.
[27] Tsuchida CA, Zhang S, Doost MS, et al. Chimeric CRISPR-Casx enzymes and guide RNAs for improved genome editing activity. Mol Cell 2022;82:1199–209.
[28] Hino T, Omura SN, Nakagawa R, et al. An AsCas12f-based compact genome-editing tool derived by deep mutational scanning and structural analysis. Cell 2023;186:4920–35.
[29] Kong X, Zhang H, Li G, et al. Engineered CRISPR-OsCas12f1 and RhCas12f1 with robust activities and expanded target range for genome editing. Nat Commun 2023;14:2046.
[30] Su M, Li F, Wang Y, et al. Molecular basis and engineering of miniature Cas12f with c-rich pam specificity. Nat Chem Biol 2023;20:180–9.
[31] Kim DY, Lee JM, Moon SB, et al. Efficient CRISPR editing with a hypercompact Cas12f1 and engineered guide RNAs delivered by adeno-associated virus. Nat Biotechnol 2022;40:94–102.
[32] Wang Y, Wang Y, Pan D, et al. Guide RNA engineering enables efficient CRISPR editing with a miniature syntrophomonas palmitatica Cas12f1 nuclease. Cell Rep 2022;40:111418.
[33] Xu X, Chemparathy A, Zeng L, et al. Engineered miniature CRISPR-Cas system for mammalian genome regulation and editing. Mol Cell 2021;81:4333–45.
[34] Bigelyte G, Young JK, Karvelis T, et al. Miniature type V-F CRISPR-Cas nucleases enable targeted DNA modification in cells. Nat Commun 2021;12:6191.
[35] Wu T, Liu C, Zou S, et al. An engineered hypercompact CRISPR-Cas12f system with boosted gene-editing activity. Nat Chem Biol 2023;19:1384–93.
[36] Zhang H, Kong X, Xue M, et al. An engineered xCas12i with high activity, high specificity and broad PAM range. Protein cell 2023;14:543.
[37] Chen Y, Hu Y, Wang X, et al. Synergistic engineering of CRISPR-Cas nucleases enables robust mammalian genome editing. Innovation (Camb) 2022;3:100264.
[38] Escobar M, Li J, Patel A, et al. Quantification of genome editing and transcriptional control capabilities reveals hierarchies among diverse CRISPR/Cas systems in human cells. ACS Synth Biol 2022;11:3239–50.
[39] Wang Y, Qi T, Liu J, et al. A highly specific CRISPR-Cas12j nuclease enables allele-specific genome editing. Sci Adv 2023;9:eabo6405.
[40] Duan Z, Zhang X, Zhang JT, et al. Molecular basis for DNA cleavage by the hypercompact Cas12j-SF05. Cell Discov 2023;9:117.
[41] Sun A, Li CP, Chen Z, et al. The compact Casπ (Cas12l) 'bracelet' provides a unique structural platform for DNA manipulation. Cell Res 2023;33:229–44.
[42] Chen W, Ma J, Wu Z, et al. Cas12n nucleases, early evolutionary intermediates of type V CRISPR, comprise a distinct family of miniature genome editors. Mol Cell 2023;83:2768–80.
[43] Xiang G, Li Y, Sun J, et al. Evolutionary mining and functional characterization of TnpB nucleases identify efficient miniature genome editors. Nat Biotechnol 2024;42:745–57.
[44] Jiang K, Lim J, Sgrizzi S, et al. Programmable RNA-guided DNA endonucleases are widespread in eukaryotes and their viruses. Sci Adv 2023;9:eadk0171.
[45] Clement K, Rees H, Canver MC, et al. CRISPResso2 provides accurate and rapid genome editing sequence analysis. Nat Biotechnol 2019;37:224–6.
[46] Tsai SQ, Zheng Z, Nguyen NT, et al. GUIDE-seq enables genome-wide profiling of off-target cleavage by CRISPR-Cas nucleases. Nat Biotechnol 2015;33:187–97.
[47] Liu Y, Yin J, Gan T, et al. PEM-seq comprehensively quantifies DNA repair outcomes during gene-editing and DSB repair. STAR Protoc 2022;3:101088.
[48] Vichai V, Kirtikara K. Sulforhodamine B colorimetric assay for cytotoxicity screening. Nat Protoc 2006;1:1112–6.
[49] Altae-Tran H, Kannan S, Demircioglu FE, et al. The widespread IS200/IS605 transposon family encodes diverse programmable RNA-guided endonucleases. Science 2021;374:57–65.
[50] Brunet E, Simsek D, Tomishima M, et al. Chromosomal translocations induced at specified loci in human stem cells. Proc Natl Acad Sci USA 2009;106:10620–5.
[51] Kim DG, Gu B, Cha Y, et al. Engineered CRISPR-Cas9 for *Streptomyces* sp. genome editing to improve specialized metabolite production. Nat Commun 2025;16:874.
[52] Jin M, Lin J, Zhang Y, et al. enOsCas12f1-mediated exon skipping for Duchenne muscular dystrophy therapy in humanized mouse model. J Genet Genomics 2024;51:256–9.
[53] Dong D, Ren K, Qiu X, et al. The crystal structure of Cpf1 in complex with CRISPR RNA. Nature 2016;532:522–6.
[54] Xun G, Zhu Z, Singh N, et al. Harnessing noncanonical crRNA for highly efficient genome editing. Nat Commun 2024;15:3823.
[55] Zuo E, Sun Y, Yuan T, et al. A rationally engineered cytosine base editor retains high on-target activity while reducing both DNA and RNA off-target effects. Nat Methods 2020;17:600–4.